

# The temporal dynamics of lncRNA *Firre*-mediated epigenetic and transcriptional regulation

Received: 21 September 2023

Accepted: 10 July 2024

Published online: 09 August 2024



Christian Much<sup>1</sup>, Erika L. Lasda<sup>1</sup>, Isabela T. Pereira<sup>1</sup>, Tenaya K. Vallery<sup>1</sup>, Daniel Ramirez<sup>1,2</sup>, Jordan P. Lewandowski<sup>3</sup>, Robin D. Dowell<sup>1,2</sup>, Michael J. Smallegan<sup>1,2</sup>✉ & John L. Rinn<sup>1,4</sup>✉

Numerous studies have now demonstrated that lncRNAs can influence gene expression programs leading to cell and organismal phenotypes. Typically, lncRNA perturbations and concomitant changes in gene expression are measured on the timescale of many hours to days. Thus, we currently lack a temporally grounded understanding of the primary, secondary, and tertiary relationships of lncRNA-mediated transcriptional and epigenetic regulation—a prerequisite to elucidating lncRNA mechanisms. To begin to address when and where a lncRNA regulates gene expression, we genetically engineer cell lines to temporally induce the lncRNA *Firre*. Using this approach, we are able to monitor lncRNA transcriptional regulatory events from 15 min to four days. We observe that upon induction, *Firre* RNA regulates epigenetic and transcriptional states in trans within 30 min. These early regulatory events result in much larger transcriptional changes after 12 h, well before current studies monitor lncRNA regulation. Moreover, *Firre*-mediated gene expression changes are epigenetically remembered for days. Overall, this study suggests that lncRNAs can rapidly regulate gene expression by establishing persistent epigenetic and transcriptional states.

To date, dozens of long noncoding RNAs (lncRNAs) have been found to contribute to a variety of phenotypes *in vivo*<sup>1</sup>. In contrast, the gene targets directly regulated by lncRNAs resulting in these phenotypes are far less understood. Most loss- or gain-of-function studies of lncRNAs measure the transcriptome at a single time point on the order of multiple hours to days or at homeostasis (e.g., knockout models). At such timescales, it is typically observed that lncRNAs regulate hundreds to thousands of genes. Thus, the earliest or primary effects of the lncRNA regulation are obscured by layers of gene-regulatory cascades and compensation mechanisms.

This has led to a variety of mechanistic models that would require timescales of many hours to days<sup>1–19</sup>. Yet, if a lncRNA regulates gene

expression rapidly within minutes, it will limit possible mechanisms and may rule out many of the existing models of lncRNA-based regulation. Thus, determining the earliest, or most direct, regulatory targets of lncRNAs will provide a basis for resolving temporally grounded mechanistic models. Currently, we lack an understanding of the primary, secondary, and further downstream regulatory events mediated by lncRNAs in order to identify the most primary regulatory sites.

Here we set out to finely map the temporal regulatory steps mediated by a lncRNA, in *trans*, from 15 min to 4 days. We chose the lncRNA *Firre* (Functional intergenic repeating RNA element) based on the following properties: (i) *Firre* is a *trans*-acting RNA that does not regulate gene expression *in cis*; (ii) gain- and loss-of-*Firre* RNA function

<sup>1</sup>BioFrontiers Institute, University of Colorado Boulder, Boulder, CO 80303, USA. <sup>2</sup>Department of Molecular, Cellular and Developmental Biology, University of Colorado Boulder, Boulder, CO 80302, USA. <sup>3</sup>Department of Stem Cell and Regenerative Biology, Harvard University, Cambridge, MA 02138, USA.

<sup>4</sup>Department of Biochemistry, University of Colorado Boulder, Boulder, CO 80303, USA. ✉e-mail: [michael.smallegan@colorado.edu](mailto:michael.smallegan@colorado.edu); [john.rinn@colorado.edu](mailto:john.rinn@colorado.edu)

in vivo phenotypes range from lethality under lipopolysaccharide exposure to defects in hematopoiesis; (iii) *Firre* is genetically associated with human diseases<sup>20–24</sup>. Although many studies have attempted to understand the mechanism of *Firre*, these efforts have resulted in several conflicting models—a conundrum that the knowledge of *Firre*'s primary regulatory sites would help to resolve<sup>23,25–27</sup>.

To this end, we engineer an inducible *Firre* mouse embryonic stem cell (mESC) system in a *Firre* knockout and wild-type (WT) background. We monitor gene expression across 16 time points on the order of minutes, hours, and days after induction of *Firre*. Combining RNA-seq, ATAC-seq, and PRO-seq across relevant time windows, we find that *Firre* can regulate transcription in a matter of minutes. Moreover, we observe changes in epigenetic state and nascent transcription within 30 min and mature target gene product within 2 h of *Firre* induction. At longer timescales, we detect numerous gene expression changes that are likely secondary or downstream modes of gene regulation. Together, our results suggest that *Firre* functions via an RNA-based mechanism that can transduce a signal within minutes to change epigenetic state and activate gene expression that then persist for days.

## Results

### Genetically engineered mESC lines for temporal control of *Firre*

To understand the temporal and sequential regulatory role of the *Firre* lncRNA, we need to be able to control the expression of *Firre* and measure the dynamics of gene expression changes before the cell returns to homeostasis. While inducible transgenes have the advantage of determining temporally grounded regulatory events, there are several key caveats to consider when using these transgenic systems. This includes the amount of induction over physiological levels and the off-target effects of doxycycline (dox).

To control for varying levels of *Firre* induction, we generated two dox-inducible *Firre* transgene lines (Fig. 1a, Supplementary Fig. 1a). For both lines, we chose the *Firre* isoform (1.49) that was previously shown to have functional roles in vivo<sup>20</sup>. One mESC line contains an inducible *Firre* transgene in a *Firre* knockout background that we term *Firre*<sup>RESCUE</sup> (Fig. 1a). The other one has the *Firre* transgene in a WT background, termed *Firre*<sup>OE</sup>. To control for effects of dox itself in the *Firre*<sup>RESCUE</sup> line, we generated an mESC line termed *Firre*<sup>KO-CTL</sup> that lacks endogenous *Firre* and contains the *Firre* transgene but does not express the reverse tetracycline-controlled transactivator (rtTA) element (Fig. 1a, Supplementary Fig. 1b). To control for dox in the *Firre*<sup>OE</sup> line, we used WT cells. We note that the derived *Firre*<sup>RESCUE</sup> and *Firre*<sup>OE</sup> mESC lines very likely differ in their transgene copy number and localization due to random Mendelian inheritance of the transgene, controlling for potential transgene positional effects on gene regulation.

To validate *Firre* expression upon induction in our cell lines, we performed RT-qPCR using *Firre* probes detecting both endogenous and transgene *Firre* after zero and 12 h of dox treatment. In the *Firre*<sup>OE</sup> line, *Firre* expression was induced to about 2.5-fold above WT levels, while in the *Firre*<sup>RESCUE</sup> line, *Firre* expression reached WT levels after 12 h. Importantly, we did not observe any induction of *Firre* expression in the WT and *Firre*<sup>KO-CTL</sup> line (Supplementary Fig. 1c). We next wanted to determine if the knockout of *Firre*, induction of *Firre*, or exposure to dox had an effect on cellular growth or morphology. Using cell counting and brightfield microscopy, we observed no changes in mESC growth or morphology in all cell lines treated with or without dox over several days (Supplementary Fig. 1d, e). This is in contrast to a previous *Firre* knockout line we generated previously that required transfection of a Cre recombinase and resulted in cellular phenotypes possibly due to toxic effects independent of *Firre*<sup>23</sup>. We further characterized the expression of the pluripotency markers *Oct4*, *Nanog*, *Sox2*, and *Klf4* (Supplementary Fig. 1f). We observed some statistically significant changes with negligible effect sizes upon addition of dox (up to 1.3-fold for *Klf4*, less than 1.1-fold for the other markers), which are within normal ranges for pluripotent cells. Collectively, we

generated genetically defined cell lines to temporally track varying levels of *Firre* expression and identify genes that are regulated by *Firre* and not dox.

### Early *Firre*-mediated gene regulation

To test the temporal gene-expression dynamics of each of the inducible lines, we collected RNA every 30 min until 5.5 h post induction of *Firre* by addition of dox and performed RNA-seq with two replicates for each time point. In both the *Firre*<sup>RESCUE</sup> and *Firre*<sup>OE</sup> lines, we detected induction of *Firre* expression already within 30 min and peak expression at around 2 h (Fig. 1b, c). As expected, we observed varying levels of *Firre* at different time points in the *Firre*<sup>RESCUE</sup> and *Firre*<sup>OE</sup> lines. This property will further allow us to identify genes regulated by *Firre* across a spectrum of induction levels.

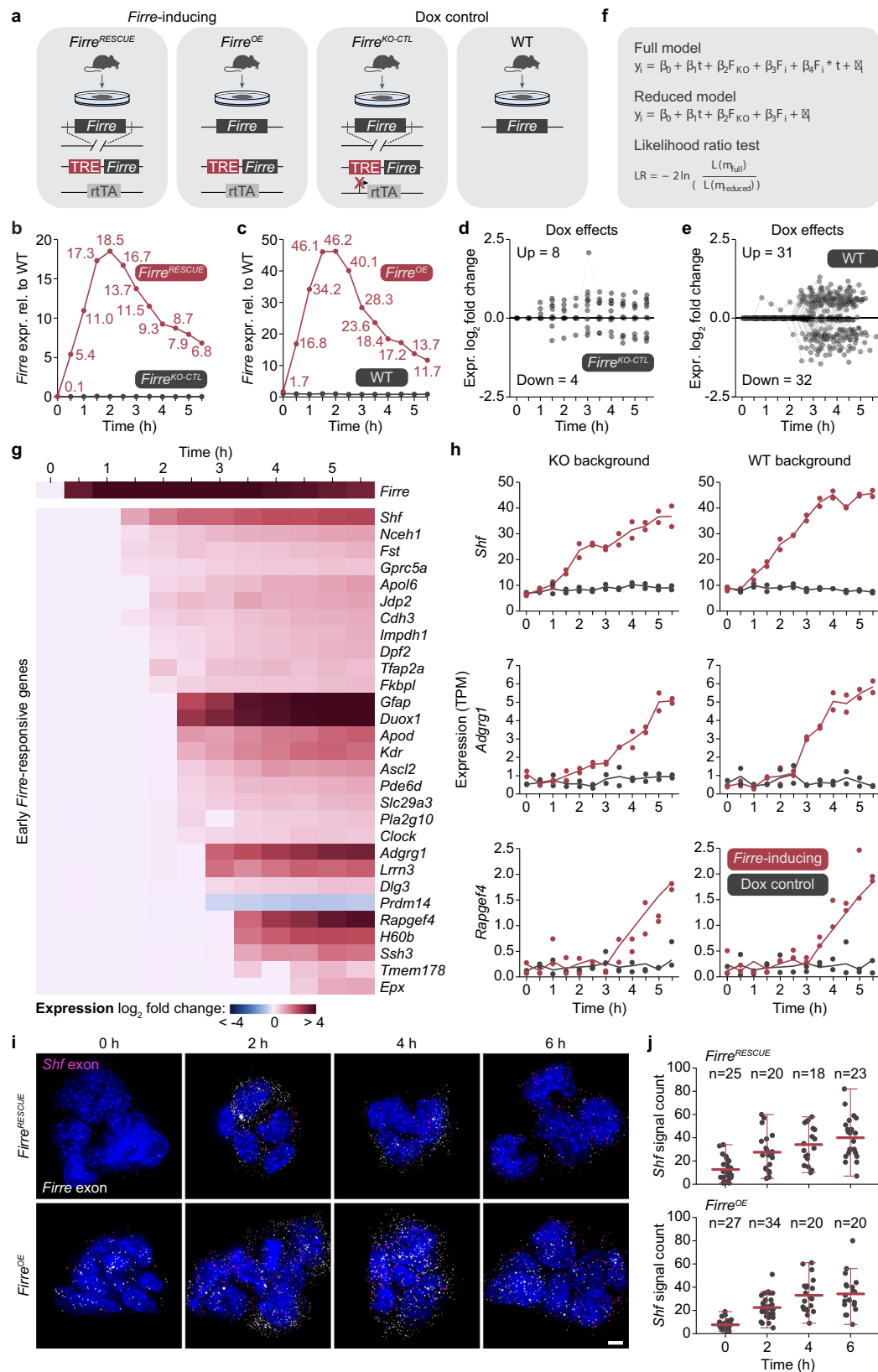
We next investigated which genes were regulated by dox itself and not due to the induction of the *Firre* lncRNA. In both *Firre*<sup>KO-CTL</sup> and WT control models, we detected very few genes that were regulated by dox alone (*Firre*<sup>KO-CTL</sup> = 12 genes, WT = 63 genes; Fig. 1d, e). Moreover, we observed that most dox-based artifacts occurred after ~2.5 h in both control models. Thus, any regulatory events observed prior would be due to the *Firre* lncRNA and not due to artifacts of the transgene system.

To generate a high-confidence list of *Firre*-mediated transcriptional regulatory events, we used a likelihood ratio test (LRT) between two regression models (Fig. 1f, see methods). The first regression model contains parameters comparing genetic background (*Firre*<sup>RESCUE</sup> and *Firre*<sup>OE</sup> models), dox control lines, and time. The second regression model lacks the dox control lines and models genetic background and time. Thus, this conservative approach requires target genes to change significantly in time, in both WT and KO background, and not due to dox. Using our conservative LRT statistical approach, we identified *Firre* as a positive control as well as 29 early *Firre*-responsive genes concordantly regulated in both *Firre* WT and KO backgrounds ( $P < 0.05$ , |fold change| > 1.5; Fig. 1g, h). Notably, all but one (*Prdm14*) of these genes were upregulated, starting to increase in expression in 1.5–4.5 h (Fig. 1g, h). Collectively, we identified a conservative cohort of genes that are the earliest and most robust responders to the induction of *Firre* RNA at different levels in WT and KO backgrounds.

While our control cell lines account for dox, they do not control for the role of the rtTA protein after dox activation. To ensure that the early *Firre* target genes are not artifacts of rtTA activation by dox, we analyzed gene expression data in mESCs with a dox-inducible Nanog transgene generated by Heurtier et al.<sup>28</sup>. We found that none of the early *Firre*-responsive genes changed significantly upon activation of rtTA by dox treatment. This result indicates that the early *Firre* targets were not induced as an artifact of rtTA activation but rather due to the *Firre* RNA (Supplementary Fig. 2a).

In addition to the dox controls above, we further wanted to validate the temporal regulatory events by single molecule RNA FISH (smRNA FISH). We chose *Shf* as a rapid and robust responder and designed a complementary exon probe set to monitor its RNA abundance and localization across time. We tested 0, 2, 4, and 6-h time points after *Firre* induction in *Firre*<sup>RESCUE</sup> and *Firre*<sup>OE</sup> lines. In both cell lines, we observed a continuous increase in the expression of *Shf* after the induction of *Firre*, independently validating our RNA-seq results with an orthogonal methodology (Fig. 1i, j).

Based on previous studies that found that *Firre* can mediate topological interactions to regulate gene expression<sup>23,27</sup>, we further used smRNA FISH to determine if the *Firre* transgene locus was in proximity to these sites. For this purpose, we measured the distance of the *Firre* transgene locus (marked by exon probes and apparent as a 'cloud') from the *Shf* locus (marked by intron probes) across the 0, 2, 4, and 6-h time points used above during which *Shf* is induced by *Firre*. We did not observe the *Firre* transgene in proximity to the *Shf* locus nor increase in proximity through time (Supplementary Fig. 2b, c).



Next, we quantified if nucleoplasmic *Firre* molecules (marked by exon probes and apparent as individual spots) were in proximity to the *Shf* locus in both *Firre*<sup>RESUE</sup> and *Firre*<sup>OE</sup> lines. We found that *Firre* RNA molecules were on average more than one micron away from the *Shf* locus and remained so despite increased expression of *Firre* and *Shf* (Supplementary Fig. 2b, d). To determine if this finding can be

extended to the other *Firre* targets, we further analyzed previous RNA proximity data (RAP)<sup>23</sup> and investigated whether the *Firre* RNA was bound in proximity to any of its target genes. We did not observe any direct RNA binding proximal to the 29 early target genes, with *Rapgef4* constituting the closest *Firre* binding event at 800 kb from its promoter (Supplementary Fig. 2e). This is in line with the fact that the

**Fig. 1 | Temporal gene regulation in *Firre* transgene mESC lines.** **a** Schematic showing the mouse blastocyst-derived mESC lines used in this study. The *Firre*<sup>RESCUE</sup> and *Firre*<sup>OE</sup> cell lines contain a dox-inducible *Firre* transgene in a *Firre* KO and WT background, respectively. The *Firre*<sup>KO-CTL</sup> and WT cell lines do not induce *Firre* expression and serve as dox controls. **b, c** *Firre* expression levels in the *Firre*<sup>RESCUE</sup> (**b**) and *Firre*<sup>OE</sup> (**c**) line (red) as well as the *Firre*<sup>KO-CTL</sup> (**b**) and WT (**c**) line (black) across time after the addition of dox as measured by RNA-seq. Numbers indicate fold expression changes over *Firre* WT levels at each time point. **d, e** Expression log<sub>2</sub> fold change of significantly differentially expressed genes that are affected by dox treatment in the *Firre*<sup>KO-CTL</sup> (**d**) and WT (**e**) control cell line. Fold changes are relative to the zero-time point. **f** Linear model to derive genes that are significantly

differentially regulated upon *Firre* transgene induction and not due to dox treatment (likelihood ratio test). **g** Heatmap of gene expression changes of early *Firre*-responsive genes over time as determined by the linear model in (**f**). **h** Gene expression changes of representative genes due to *Firre* in *Firre*-inducing (red) but not in dox control (black) cells of *Firre* WT and KO background. **i** Maximum intensity projections of smRNA FISH images for *Shf* exon (magenta) and *Firre* exon signals (white) in *Firre*<sup>RESCUE</sup> and *Firre*<sup>OE</sup> mESC colonies after 0, 2, 4, and 6 h of dox treatment. Nuclei are stained with Hoechst (blue), *Firre* exon in white, and *Shf* exon in magenta. Scale bar is 5  $\mu$ m. **j** Quantification of *Shf* exon FISH signals in *Firre*<sup>RESCUE</sup> and *Firre*<sup>OE</sup> mESCs. The horizontal line indicates the mean and the vertical line the non-outlier range of quantified cells.

29 early target genes are randomly distributed over 16 chromosomes, rendering it unlikely that the *Firre* transgene forms *trans*-chromosomal contacts with all those loci. Thus, the previously observed topological and direct RNA associations may occur after homeostasis is achieved and not during the direct regulation of these sites.

*Firre* has further been implicated in the regulation of the repressive histone H3 lysine 27 trimethylation (H3K27me3) mark in non-stem cells<sup>27</sup>. To test this mechanism in stem cells, we designed a strategy to examine the influence of the Polycomb repressive complex 2 (PRC2) that controls H3K27me3 states and used GapmeRs to knockdown the PRC2 subunits *Ezh2*, *Suz12*, *Jarid2*, and *Aebp2* in *Firre*<sup>OE</sup> mESCs. After 24 h of GapmeR exposure, the *Firre* transgene was induced by dox for 6 h (Supplementary Fig. 3a). We reasoned that if PRC2 was required for *Firre*-mediated gene expression regulation, knockdown of PRC2 subunits would abolish the upregulation of the early *Firre*-responsive genes *Adgrg1* and *Shf* (Supplementary Fig. 3b). We validated the effective depletion of the investigated PRC2 subunits at the RNA and protein level (Supplementary Fig. 3c). Using a non-targeting control (NTC) GapmeR, we confirmed the induction of *Firre* and the concomitant upregulation of the *Firre* responders *Adgrg1* and *Shf* after the addition of dox, while the non-*Firre* target *Tug1* remained unchanged (Supplementary Fig. 3d). However, we found that depletion of any of the PRC2 subunits did not significantly decrease the upregulation of the tested *Firre*-responsive genes (Supplementary Fig. 3d). To further investigate the importance of H3K27me3 in *Firre*-mediated gene regulation, we performed ChIP-seq for H3K27me3 in all four cell lines treated with dox for zero and 48 h. Of the total 102,957 peaks detected, only one changed significantly in response to *Firre* (*Rapgef4*, Supplementary Fig. 3e, f). This suggests that *Firre*'s target gene regulation is likely not mediated by PRC2 and H3K27me3 in mESCs and that this mechanism is rather context specific.

Collectively, these results point to 29 high-confidence genes that are rapidly and robustly changing upon exposure to varying levels of *Firre* RNA across time and not due to dox, rtTA, proximity to the *Firre* transgene locus, nor PRC2-mediated H3K27me3. Thus, we have likely identified the primary regulatory sites of the *Firre* lncRNA that occur at timescales hitherto unstudied.

### Temporal dynamics of epigenetic regulation by *Firre*

Based on our finding that *Firre* regulates primary target sites within a few hours, we further hypothesized that changes to epigenetic states may occur prior to these transcriptional changes. To test this hypothesis, we performed ATAC-seq every 30 min for 2.5 h across the four different mESC lines. Importantly, we found no ATAC peaks significantly changing in time due to dox ( $P < 0.05$ ) in this early time frame. Testing for differential accessibility by comparing all conditions in which *Firre* was induced (time point > 0 in *Firre*<sup>RESCUE</sup> and *Firre*<sup>OE</sup> lines) to conditions in which the *Firre* transgene was not induced (WT and *Firre*<sup>KO-CTL</sup> lines; zero-time point in *Firre*<sup>RESCUE</sup> and *Firre*<sup>OE</sup> lines), we identified a total of 55 ATAC peaks that changed ( $P < 0.05$ ) in response to *Firre*'s induction (Fig. 2a, Supplementary Fig. 4a). Of these 55 peaks, 51 (93%) were associated with an increase in chromatin accessibility over the time course (Fig. 2a, Supplementary

Fig. 4a), which is consistent with the observed subsequent transcriptional activation.

Next, we wanted to determine how many of the differentially accessible ATAC peaks were in proximity to genes changing in expression upon *Firre* induction. We identified ten differentially accessible ATAC peaks within 50 kb of the transcription start site (TSS) of early *Firre*-responsive genes and *Firre* itself (Fig. 2b). One of these peaks was in proximity to two neighboring genes, *Duox1* and *Shf*, which both increased in expression. Analysis of the ATAC-seq peak center location relative to the TSS for the ten genes (excluding *Firre*) revealed that all but one ATAC peaks were downstream of the TSS (Fig. 2c). The gene *Rapgef4*, for example, rapidly gained ATAC peak signals within its first intron at a proximal enhancer element (Fig. 2d, Supplementary Fig. 4b). Together, these results suggest that the *Firre* RNA is sufficient to alter chromatin accessibility within 30 min.

We next wanted to define the timing of chromatin accessibility and gene expression changes upon *Firre* induction. To this end, we compared the temporal dynamics of ATAC- and RNA-seq changes side by side and identified eleven genes (including *Firre*) that had concomitant changes in ATAC- and RNA-seq, while the other 18 genes may have longer range chromatin or accessibility changes or were already accessible. Moving forward we focus on these eleven genes as they have multiple characteristics of bona fide direct targets. Notably, for all eleven genes (including *Firre*), chromatin accessibility increased already within 30 min and in all cases preceded gene expression changes (Fig. 2e). Importantly, within this time window, *Firre* was expressed at or near WT levels in both *Firre*-inducing cell lines. To formalize the observed temporal dynamics, we created a meta-profile of ATAC- and RNA-seq signal changes for these genes (Fig. 2f). We found that, on average, ATAC peaks and RNA abundance reached half-maximal at 47 min and 104 min, respectively. Together, these data provide evidence that *Firre* rapidly increases chromatin accessibility which in turn leads to an upregulation of gene expression.

### *Firre* regulates RNA transcription within minutes

Our results above demonstrate that the *Firre* RNA can induce changes in chromatin within 30 min, suggesting that transcriptional changes might be occurring on short timescales as well. As poly(A) RNA-seq is only detecting mature transcripts, its temporal resolution is limited by pre-mRNA processing time. Therefore, to identify transcriptional regulatory events at or prior to 30 min, we performed PRO-seq which measures nascent transcription with a temporal resolution on the order of minutes<sup>29</sup>. Importantly, at these time points, *Firre* is induced to near-WT levels in the *Firre*<sup>RESCUE</sup> line. Thus, any regulatory events observed are likely not a consequence of *Firre* overexpression, but rather due to *Firre* RNA expressed at its physiological levels.

To examine the earliest and most direct regulatory effects of *Firre*, we performed PRO-seq in the *Firre*<sup>RESCUE</sup> model at 0, 15, and 30 min post addition of dox in biological triplicates. We first used Tfit<sup>30</sup> to determine the number of bidirectional regions indicative of transcriptional activity (Fig. 3a). This resulted in a total of 29,842 sites of bidirectional transcription. Most of these sites of RNA polymerase activity remained unchanged, including the *Ep300* promoter (Fig. 3b). However, at genes



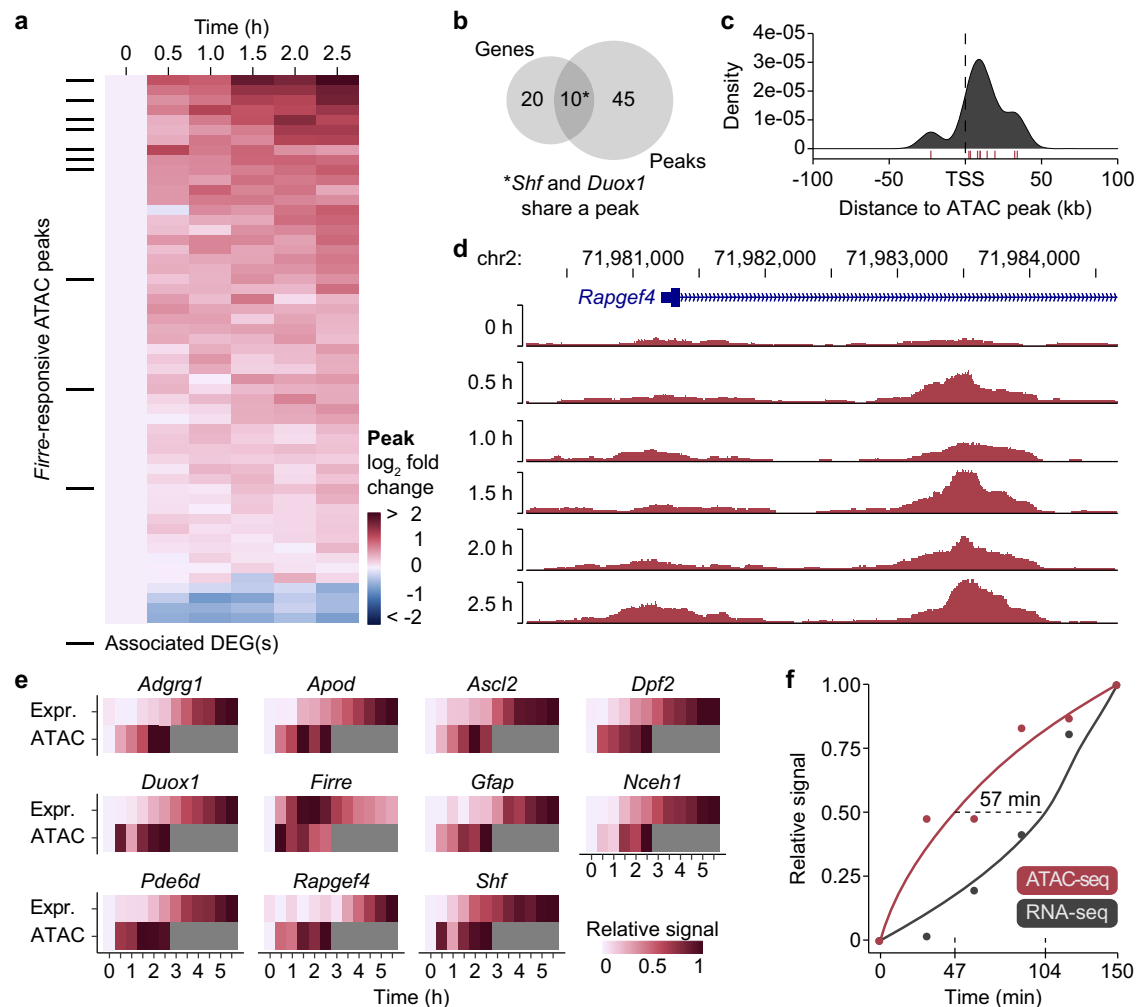


**Fig. 2 | Changes in chromatin accessibility upon induction of *Firre*.** **a** Heatmap showing chromatin accessibility  $\log_2$  fold changes across time. Increased chromatin accessibility relative to the zero-time point is depicted in shades of red, decreased chromatin accessibility in blue. Black tick marks indicate differentially expressed genes. **b** Venn diagram showing the overlap of early *Firre*-responsive genes and *Firre*-mediated chromatin accessibility sites. **c** TSS metaplot of the density of ATAC-seq peak centers relative to *Firre*-responsive gene TSSs. Red tick

marks indicate the peak centers. **d** Genome browser tracks of chromatin accessibility changes across time within *Rapgef4* in *Firre*<sup>RESCUE</sup> cells. **e** Heatmap of chromatin accessibility and gene expression changes at each time point after induction of *Firre*. Time points where chromatin accessibility was not measured are indicated in gray. **f** Plot of chromatin accessibility (red) and gene expression (black) signal relative to the maximum measured over time. The dashed line represents the time difference in half-maximum values.

differentially expressed at the mature RNA level, such as *Shf* and *Duox1*, we interestingly observed changes in nascent transcription within 15 min (Fig. 3b).

To determine differentially expressed bidirectional sites globally, we performed an LRT by comparing a full model with the time component to a reduced model representing the mean expression, resulting in 550 differentially expressed bidirectional regions ( $\text{padj} < 0.05$ ;  $|\text{fold change}| \geq 1.5$ ). In contrast with the observed changes in mature RNA being predominantly gene activation, sites of bidirectional nascent transcription were up- and downregulated (upregulated = 248, downregulated = 302; Fig. 3c, Supplementary Fig. 5a). Most bidirectional sites of nascent transcription responded transiently at 15 min, followed by a return toward pre-induction levels by 30 min. However, 41 of the 550 differentially expressed bidirectionals continued a monotonic trend. Of those, *Apod*, *Shf*, and *Duox1* had monotonically increasing bidirectional signals co-located within increasing ATAC-seq peaks (Fig. 3d). Correspondingly, these regions exhibited some of the largest expression fold changes in mature transcripts. Thus, we can now place *Firre*-regulatory events in temporal sequence of primary chromatin accessibility targets that lead to the subsequent mRNA changes shortly after.

To assess the concordance between nascent transcription and RNA-seq expression changes, we calculated the differential expression for nascent transcripts along the gene body. We detected 18 of the 29 early *Firre* responders as significantly differentially expressed at the nascent transcript level ( $\text{padj} < 0.05$ , Fig. 3e). The five genes with the earliest detected changes at 1.5 h in RNA-seq (*Shf*, *Nceh1*, *Fst*, *Gprc5a*, and *Cdh3*) all had increasing nascent transcription along the gene body by 30 min, and four of those five genes were significantly upregulated one to 2 h later ( $\text{padj} < 0.05$ , Fig. 3e, Supplementary Fig. 5b). In summary, we identified many sites that rapidly and transiently respond to *Firre*, with only some resulting in persistent nascent and mature expression changes. This underscores the importance of multiple genomic scale approaches to home in on bona fide lncRNA gene targets that exhibit persistent opening of chromatin, induction of nascent transcription and robust activation of the target gene's mature transcript.

#### *Firre*-mediated transcriptional regulation persists for days

While the goal of this study is to identify robust, reproducible, and primary regulatory sites of *Firre*, we also wanted to determine how long these regulatory changes last. To this end, we performed an RNA-seq time course for 0, 12, 24, 48, and 96 h in biological triplicate for all

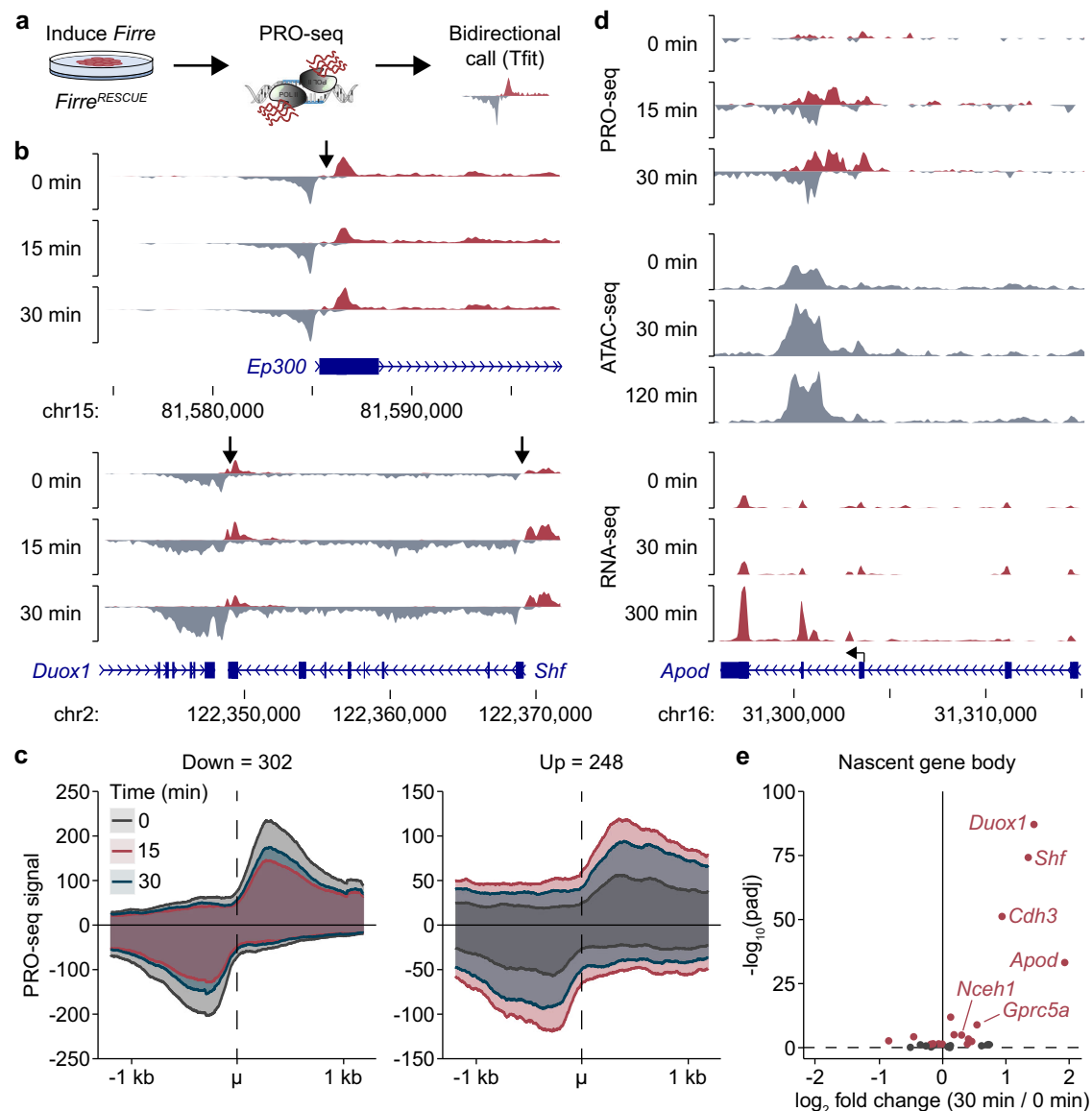


**Fig. 3 | Rapid nascent transcriptional changes upon *Firre* induction.** **a** Schematic of PRO-seq experimental setup. **b** Genome browser tracks of bidirectional transcription of genes that were (*Shf*, *Duox1*) and were not (*Ep300*) differentially expressed upon *Firre* induction. Red and gray areas indicate reads on the plus and minus strand, respectively. Arrows denote the bidirectional center. **c** Metaplot of PRO-seq signal at the differentially expressed sites of bidirectional transcription

( $\text{padj} < 0.05$ ,  $n = 550$ , Wald test) around the bidirectional center ( $\mu$ ) at the 0-, 15-, and 30-min time points. **d** Genome browser tracks showing the regulatory events at the *Apod* locus upon *Firre* induction. The arrow indicates an internal TSS. **e** Volcano plot of the  $\log_2$  fold changes of nascent transcription over the gene body at 30 vs 0 min. Genes with  $\text{padj} < 0.05$  (Wald test) are indicated in red.

four cell lines at each time point. We used a similar LRT that requires genes to significantly change across time in both *Firre*<sup>RESCUE</sup> and *Firre*<sup>OE</sup> lines and neither in *Firre*<sup>KO-CTL</sup> nor WT cells treated with dox. We observed that in both the *Firre*<sup>RESCUE</sup> and *Firre*<sup>OE</sup> lines, *Firre* was induced highest at 12 h and then remained at much lower levels up to 96 h (Fig. 4a, b).

Next, we wanted to determine if the early *Firre* target genes continued to be regulated on the timescale of days. We focused on the ten genes that had immediate changes in chromatin accessibility, activation of nascent transcription and subsequent mRNA activation 2 h later. Strikingly, we observed that all ten genes were induced to maximum levels within 12 h and persisted at or close to these levels for 96 h (Fig. 4c). This suggests that the early epigenetic changes induced by *Firre* are remembered for days.

We further utilized this longer time course to identify the cascade of secondary and tertiary regulatory events that subsequently

followed from the 10–29 primary sites of *Firre* regulation. We focused on the *Firre*<sup>RESCUE</sup> and *Firre*<sup>KO-CTL</sup> cell lines and applied a similar LRT that requires genes to be significantly changed across time and not dox. We observed 414 genes significantly regulated by *Firre* and not dox across time ( $P < 0.05$ ;  $|\text{fold change}| \geq 1.5$ ; Fig. 4d, Supplementary Fig. 6a, b). Thus, we found a large expansion of the gene list from 10–29 genes at the earliest measurable time points to 414 genes at the longer time frames. These results demonstrate the importance of temporal studies as the primary early targets persist at longer time points, but would be hard to identify in the wake of over 400 genes changing by 12–96 h—a time frame often used in lncRNA studies.

We wanted to further leverage our *Firre*<sup>RESCUE</sup> line to determine the extent to which the *Firre* transgene restored gene expression to WT levels—or rescued the knockout expression phenotype. Specifically, we compared the genes that were significantly differentially expressed in response to *Firre*'s induction with those that were significantly

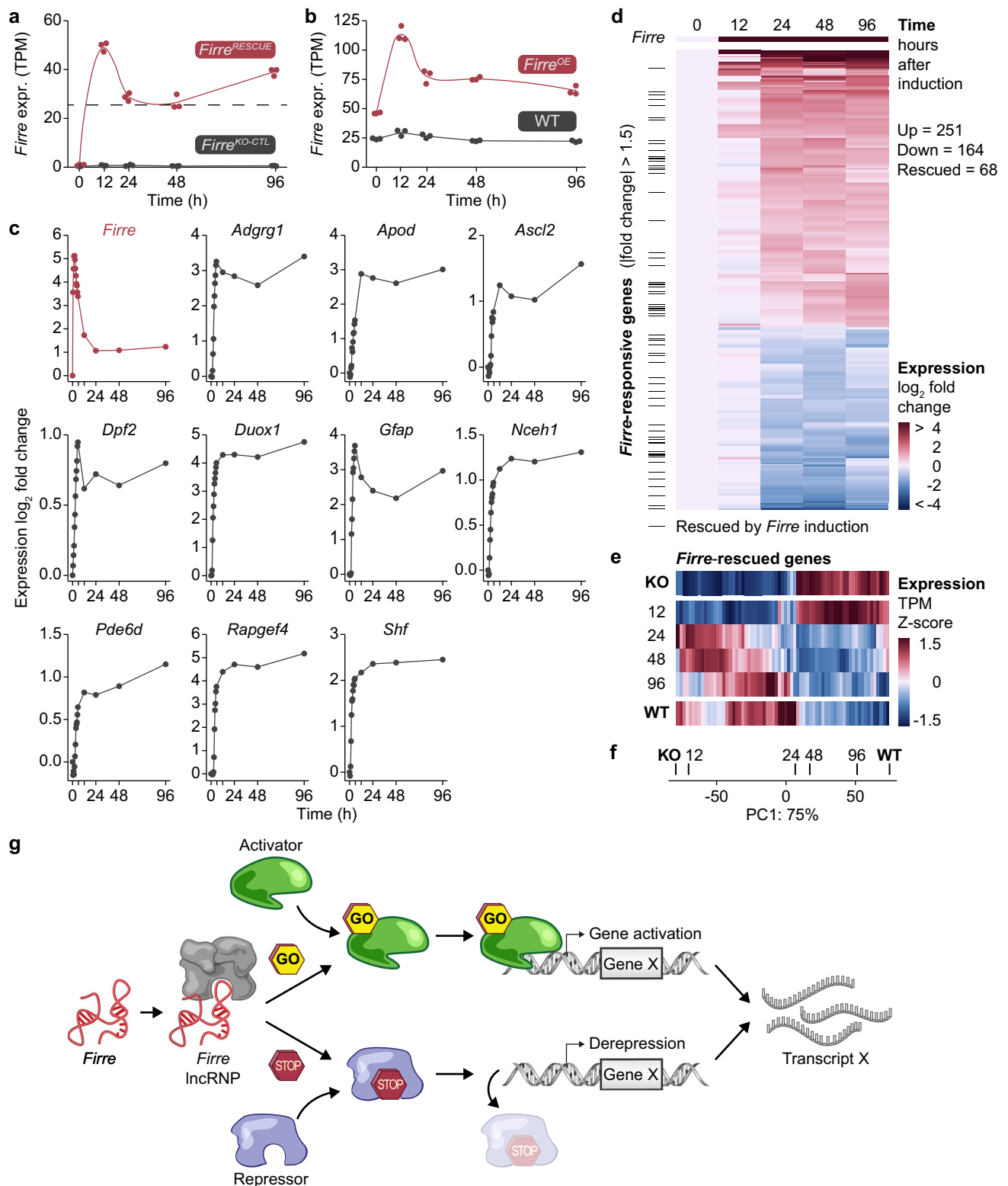


**Fig. 4 | Persistence of *Firre*-mediated transcriptional regulation over time.**

**a, b** Expression levels of *Firre* in *Firre*<sup>RESCUE</sup> (red) and *Firre*<sup>KO-CTL</sup> mESCs (black) (**a**) and *Firre*<sup>OE</sup> (red) and WT mESCs (black) (**b**) across time after the addition of dox as measured by RNA-seq. The dashed line indicates *Firre* WT expression levels. **c** Individual gene plots showing the log<sub>2</sub> expression fold change in the *Firre*-inducing cell lines compared to the zero-time point for all measured time points. **d** Heatmap of the expression fold changes of significantly differentially expressed genes over time upon *Firre* induction independent of dox effects. Black tick marks represent genes whose expression was rescued, i.e., that were downregulated in the knockout and upregulated upon transgene induction, or vice versa. **e** Heatmap of

the expression of 68 rescued genes across each time point. Top and bottom heatmap represent the *Firre*<sup>KO</sup> and WT expression levels, respectively. The heatmaps in between represent the temporal timing of when genes are rescued. **f** PCA of the rescued gene expression levels in WT, *Firre*<sup>KO</sup> and *Firre*<sup>RESCUE</sup> cells at each time point. The primary component PC1 that represents 75% of the variation in the data is plotted. **g** Model of *Firre*-mediated gene regulation depicting *Firre* forming a lncRNA by binding to an unknown protein, which either engages an activator protein to bind to chromatin or evicts a repressor protein from chromatin, ultimately leading to the upregulation of *Firre* target genes.

differentially expressed in uninduced *Firre*<sup>KO</sup> and WT cells. Of the 414 genes responding to *Firre*'s induction, a significant number of genes (102) overlapped with the 921 differentially regulated genes in the *Firre*<sup>KO</sup> vs WT comparison (hypergeometric  $P = 5.79 \times 10^{-70}$ , Supplementary Fig. 6c, d). We defined genes as rescued when they were downregulated in the *Firre*<sup>KO</sup> cells and upregulated in the *Firre*<sup>RESCUE</sup> cells, or vice versa, and reverted to  $\pm 20\%$  of WT levels. Of the 102 overlapping genes, 68 fit these rescue criteria (Supplementary Fig. 6e). We next determined the temporal dynamics of this gene expression restoration. Principal component analysis (PCA) showed an initial shift toward rescued gene expression levels between twelve and 24 h (Fig. 4e, f). Thus, early primary targets lead to a transcriptional cascade of over 400 genes, including those that are restored to WT levels.

Lastly, we wanted to determine if the genes rescued by *Firre* had common gene functions. To this end, we performed enrichment analyses using Enrichr<sup>31,32</sup>. We first examined the Reactome pathway and found that the rescued genes are enriched for several common biological pathways. Interestingly, we noted that DNA methylation was the second most significant category (Supplementary Fig. 6f). We further observed enrichment of blood-related pathways which is consistent with *Firre* phenotypes observed in our previous in vivo studies<sup>20</sup>. Collectively, these enriched pathways provide some insight into the regulatory roles of the larger cohort of over 400 genes regulated by *Firre*. Next, we utilized the 'TF Perturbations Followed by Expression' analysis to find possible transcription factor pathways involved. Strikingly, the rescued genes were most significantly enriched in the transcription factor *Prdm14* knockout gene set (Supplementary Fig. 6g). This is of note as *Prdm14* is the only primary target that was downregulated by *Firre* in our list of 29 early responders and would be consistent with *Firre* downregulating *Prdm14* and in turn a cascade of genes being rescued by *Firre*.

Collectively in this study, we present a set of experiments that tracks the regulatory effects of the *Firre* lncRNA at its target sites from the earliest measurable changes in transcriptional activity, through changes in chromatin accessibility, to increased expression of mature RNA products which then persist through the latest time point at 4 days.

## Discussion

Knowing the primary targets of any regulatory element is critical to understand its mechanisms. Understanding when, where, and how much gene regulation occurs allows these sites to be assayed to identify the corresponding molecular componentry underlying this regulation. For example, a common first step in understanding how a transcription factor functions is to identify the primary targets and subsequent temporal dynamics of gene regulation. These primary sites can be further used to assay for a variety of functional and mechanistic studies underlying transcription factor regulation.

Similarly, lncRNAs have been implicated in regulating a variety of transcriptional programs. However, most studies measure gene-regulatory events on the timescale of many hours to days. Thus, it is difficult to discern primary regulatory sites from secondary, tertiary, and more downstream ripple events. In contrast, it is well known that transcription factors regulate their primary targets on the scale of minutes—a timescale not explored for lncRNAs prior to this study<sup>29,33–45</sup>. To begin to determine the timescales at which lncRNAs regulate transcription, we combined several genome-scale approaches and employed genetically defined models and fine-grained temporal resolution from minutes to days. We reasoned that the earliest RNA-mediated regulatory events are the most direct or primary sites of lncRNA regulation.

Using our temporally controlled approach, we made several findings with implications for understanding lncRNA-mediated gene regulation. First, we were somewhat surprised at how rapidly the gene-regulatory events unfolded upon induction of the *Firre* lncRNA. We

observed that robust epigenetic and transcriptional changes occurred within 30 min—a time frame hitherto unstudied in lncRNA functional studies.

Second, lncRNAs have been implicated in a variety of epigenetic mechanisms, but we lack an understanding of the temporal relationships to subsequent regulatory events. Our findings suggest that *Firre* is sufficient to induce epigenetic changes, such as chromatin accessibility, prior to the activation of genes near these sites and that these regulatory events last for days. Thus, our results further reinforce the hypothesis that lncRNAs are epigenetic regulators.

Third, our study underscores the importance of understanding the temporal dynamics underlying lncRNA regulation. Specifically, in order to determine primary targets, it was paramount to measure gene-regulatory events within a few hours of *Firre* induction. The 10–29 *Firre* target genes would have otherwise been impossible to pinpoint among the 400 or more secondary and tertiary targets observed after 12 h. Collectively, our study demonstrates that lncRNAs could act early at a few sites that, in turn, result in larger transcriptional regulatory cascades. This is akin to what is known for transcription factors.

Lastly, observing lncRNA-mediated gene regulation across time leads to several biological insights. For example, within 30 min, *Firre* induces chromatin accessibility and nascent transcription at the *Adgrg1* locus—a gene causally linked to the human disease polymicrogyria<sup>46</sup>. Interestingly, *Firre* has also been causally linked to polymicrogyria<sup>21</sup>, suggesting a possible link between *Firre* and *Adgrg1* in human disease. Moreover, *Adgrg1* as well as *Apod* are primary targets of *Firre* involved in adipogenesis<sup>47</sup>, a cell process in which *Firre* is required<sup>48</sup>. Thus, the early or direct targets may harbor clues into how *Firre* mediates cellular differentiation and human disease. On longer timescales, *Firre* induction rescues genes lost or gained in the knockout background. These genes include DNA methylation pathways that may explain how so few primary targets result in larger gene expression changes. Notably, the rescued genes significantly overlap with previous studies that knockout *Prdm14*—the only primary target downregulated by *Firre*, suggesting that one of the key primary events mediated by *Firre* is downregulation of *Prdm14*. In summary, the time and target gene functions raise temporally grounded hypotheses of how *Firre* may function in cellular differentiation and human disease.

While temporally controlled transgene systems afford numerous insights outlined above, there are several caveats that also need to be considered. Gene expression artifacts could be caused by the exposure to dox and activated rtTA. To account for these possibilities, we exposed control cell lines that did not express rtTA to dox, and referred to an existing study to rule out any gene expression changes that could be caused by dox and activated rtTA. A second important consideration is the overexpression of *Firre* above WT levels. One way of mitigating this issue is to induce *Firre* at different levels and only consider significant regulatory events that occur independent of the abundance of *Firre*. To this end, we used the *Firre*<sup>RESCUE</sup> and *Firre*<sup>OE</sup> lines that induce *Firre* at varying levels in each line and at each time point. Thus, we only considered genes to be regulated by *Firre* if they occurred at all levels (from near WT to overexpressed). A final indication that our results are not due to overexpression artifacts is the observation that the earliest regulatory events occurred between 15–30 min. Within 30 min, we observed robust changes in chromatin accessibility and induction of nascent transcription at these sites. In this time frame, *Firre* abundance was at or near WT levels in the *Firre*<sup>RESCUE</sup> model, suggesting that the observed epigenetic and transcriptional regulatory events are attributable to near WT levels of *Firre*. Overall, the reported primary regulatory events occurred independent of *Firre* abundance, were consistent across time, persisted for days, and did not take place in dox control lines.

The rapidity of RNA-based regulation by *Firre* likely precludes the possibility of a new mRNA being transcribed, spliced, exported,



translated, and the protein re-localized to the nucleus and, in turn, regulating epigenetic states and transcription in the timescale of 30 min. This reduces the search space toward mechanistic models that could occur in these short time frames. Regulation by *Firre* within a few minutes likely requires an existing nucleoplasmic factor that sends a rapid signal to another factor poised at the target site. Specifically, *Firre* could be activating an activator or repressing a repressor to specifically upregulate its primary target genes (Fig. 4g). We note that identifying such lncRNA-protein (lncRNP) interactions is a necessary next step towards understanding the molecular mechanisms leading to the observed rapid epigenetic and transcriptional regulatory events. Our study provides a system to temporally monitor lncRNP formation and identify specific RNA-protein interactions that are temporally congruent with regulatory events.

Cells can ‘sense’ DNA damage, heat shock, hormone exposure, and even viral RNA and transduce a signal that results in gene activation or repression within minutes<sup>29,33–43</sup>. It is therefore an intriguing possibility that lncRNAs could also rapidly regulate transcription by acting upstream in signal transduction cascades. This would be consistent with the RIG-I RNA-sensing pathway—where RIG-I binds RNA, is activated, and triggers a specified transcriptional response of a few immediate genes<sup>36</sup>. Thus, lncRNAs could also serve as allosteric adapters to activate or repress signal transduction molecules in a similar manner across a diversity of signal transduction pathways (Fig. 4g). In the case of *Firre*, we could envision an RNA-protein interaction that changes the conformation of a signaling molecule to be activated and specify a targeted transcriptional response. Finally, a nuclear localized RNA, such as *Firre*<sup>23,49</sup>, would be an ideal molecule for these rapid and fine-tuned transcriptional responses.

In summary, our ‘multi-omic’ temporal study demonstrates that *Firre* rapidly, robustly, and reproducibly regulates transcription and epigenetic states within 30 min—resulting in the activation of a cohort of target genes. These primary regulatory sites will serve as an invaluable tool for future work on elucidating the role of RNA-based transcriptional and epigenetic regulation. Based on these high-resolution temporal insights, we are now poised with the most immediate and direct primary sites of regulation by a lncRNA. We can next leverage these sites to assay the underlying molecular modalities and mechanisms of RNA-based epigenetic and transcriptional regulation.

## Methods

### Ethics statement

Mice were group-housed with a 12 h light-dark schedule at 20–23 °C and 30–50% humidity in a specific pathogen-free facility. We have complied with the ethical regulations for animal testing and research in accordance with and as approved by Harvard University’s Institutional Animal Care and Use Committee (protocol number 11-13-2).

### Derivation and culture of genetically modified mESCs

mESC derivations were performed with the assistance of Harvard’s Genome Modification Facility. Briefly, 2–5 IU of pregnant mare serum gonadotropin (PMSG) and 2–5 IU of human chorionic gonadotropin (HCG) were administered 48 h apart by intraperitoneal injection to female mice heterozygous for *Firre* (*Firre*<sup>+/-</sup>). PMSG/HCG-treated mice were set up for timed matings (1–2 per cage) with either male mice deficient for *Firre* (*Firre*<sup>-/-</sup>) or with male mice that contained an inducible *Firre* transgene in the *Firre*-deficient background (*Firre*<sup>+/y</sup>; tg-*Firre*; *CAGs-rtTA3*) as previously described<sup>20</sup>. Female mice were checked for copulation plugs the following morning. Approximately 72 h later, blastocysts were flushed out of the uterine horns from female mice with successful copulation plugs. Blastocysts with a detected cavity were selected for culture and expansion. Individual clones were screened by PCR genotyping for *Firre* WT, KO, transgene, and

*CAGs-rtTA3* alleles as described<sup>20</sup>, and one independent male cell line per genotype was derived.

mESCs were maintained on 0.1% gelatin in KnockOut DMEM (Thermo Fisher, 10829018) supplemented with 12.5% FCS (MilliporeSigma, ES-009-B), 1X GlutaMAX supplement (Thermo Fisher, 35050061), 1X non-essential amino acids (Thermo Fisher, 11140050), 100 U/mL penicillin/streptomycin (Thermo Fisher, 15140122), 100 μM 2-mercaptoethanol (Thermo Fisher, 31350010), 1 μM PD0325901 (MilliporeSigma, PZ0162-5MG), 3 μM CHIR99021 (MilliporeSigma, SML1046-5MG), and 100 U/mL LIF (MilliporeSigma, ESG1107) at 37 °C and 7.5% CO<sub>2</sub>. Cells were routinely tested for mycoplasma contamination by PCR.

Cells were treated with 1 ng/μL dox (MilliporeSigma, D9891-5G) the day after they were seeded and 1 h after the medium was changed to reduce cell stress.

### RNA isolation, quantification, and quality control

Total RNA was extracted using TRIzol lysis reagent (Thermo Fisher) and purified using the RNeasy Plus Mini Kit (Qiagen) according to the manufacturer’s instructions. RNA concentration was measured with a Qubit fluorometer (Invitrogen), and RNA quality was determined using a Bioanalyzer or TapeStation (Agilent Technologies).

### RT-qPCR

Total RNA was reverse-transcribed using the SuperScript IV First-Strand Synthesis System with random hexamers (Thermo Fisher) according to the manufacturer’s instructions. RT-qPCR samples were prepared either using TaqMan probes and the TaqMan Fast Advanced Master Mix (Thermo Fisher; *Firre* induction) or using primers and the LightCycler 480 SYBR Green I Master mix (Roche; knockdown assay) according to the manufacturer’s instructions. Primer sequences are provided in Supplementary Data 1. The *Firre* transgene probe was designed against exons 1–2 and detects both the *Firre* transgene and endogenous *Firre*. Samples were run in technical duplicates or triplicates on a Bio-Rad C1000 Touch Thermal Cycler. *C<sub>t</sub>* values were normalized against the internal controls *Gapdh* and *Actb*. Fold differences in expression levels were calculated according to the 2<sup>-ΔΔC<sub>t</sub></sup> method<sup>50</sup>.

### RNA-seq

RNA-seq libraries were prepared from 1 μg of total RNA using the TruSeq RNA Library Prep Kit v2 (Illumina) with poly(A) selection according to the manufacturer’s instructions. Multiples of twelve randomized samples were each multiplexed, pooled, and run in one HiSeq lane.

### smRNA FISH

Oligonucleotides tiling *Firre* exons (including its RRDs), *Shf* exons, and *Shf* intron 1 were designed with the Stellaris RNA FISH probe designer (LGC Biosearch Technologies, version 4.2), labeled with Quasar 570 or 670, and produced by LGC Biosearch Technologies. Probe sequences are provided in Supplementary Data 2.

Cells were seeded on cover glasses coated with 0.1% gelatin. Cover glasses were washed twice with PBS, fixed in 3.7% formaldehyde in PBS for 10 min at room temperature, and washed again twice with PBS. Cover glasses were incubated in 70% ethanol at 4 °C for at least 1 h and then washed with 1 mL of wash buffer A (LGC Biosearch Technologies) at room temperature for 5 min. Cells were hybridized with 100 μL of hybridization buffer (LGC Biosearch Technologies) containing the FISH probes at a 1:100 dilution in a humid chamber at 37 °C overnight up to 16 h. The next day, cells were washed with 1 mL of wash buffer A at 37 °C for 30 min and stained with wash buffer A containing 10 μg/mL Hoechst 33342 (Thermo Fisher) at 37 °C for 30 min. Cover glasses were washed with 1 mL of wash buffer B (LGC Biosearch

Technologies) at room temperature for 5 min, mounted with ProLong Gold (Thermo Fisher) on a glass slide, and left to cure at 4 °C overnight before proceeding to image acquisition.

Image acquisition was performed using a DeltaVision Elite wide-field microscope with an Olympus UPlanSApo 100 ×/1.40-numerical aperture oil objective lens and a PCO Edge sCMOS camera. Z-stacks of 200 nm step size capturing the entire cell colony were acquired. Images were deconvolved with the built-in DeltaVision SoftWoRx Imaging software and maximum intensity projections were created using ImageJ/Fiji. FISH spots were quantified manually using ImageJ/Fiji.

Imaris image analysis software (Bitplane) was used to quantify the distances between FISH spots. Images were prepared and FISH spots detected as previously described<sup>51</sup>. Coordinates of each *Shf* intron spot and the closest 'Ferre cloud' (identified in 3D as the brightest *Ferre* signal in the nucleus) or the five closest *Ferre* exon spots within the same cell were recorded and used to calculate their Euclidean distance from each other.

### Knockdown assays

For knockdown assays, triplicates of  $3 \times 10^5$  mESCs were seeded per well of a 6-well plate. The next day, cells were reverse transfected with 25 nM GapmeRs (Qiagen) using Lipofectamine RNAiMAX Transfection Reagent (Thermo Fisher) according to the manufacturer's instructions. After 24 h, either no dox (zero-time point) or 1 ng/μL dox (6-h time point) was added without performing a media change, and cells were harvested after 6 h for RNA and protein extraction.

### Protein extraction and western blotting

Cells were collected by trypsinization, washed with cold PBS, and incubated in lysis buffer (50 mM Tris HCl pH 7.5, 150 mM NaCl, 1% NP-40, 3 mM MgCl<sub>2</sub>, 5% glycerol, 1X protease inhibitors) for 20 min on ice. Protein extracts were collected as supernatant after centrifugation at 14,000 × g for 10 min at 4 °C, resolved on an Any kD Mini PROTEAN TGX Precast Protein Gel (Bio-Rad) and transferred to a nitrocellulose membrane (Millipore) via wet transfer in the cold room overnight. Membranes were blocked in 5% milk in TBS-T (TBS with 0.1% Tween 20) and probed with anti-EZH2 (D2C9), anti-SUZ12 (D39F6), anti-JARID2 (D6M9X), anti-AEBP2 (D7C6X), or anti-GAPDH antibody (14C10, all Cell Signaling Technology) at a dilution of 1:1000 in blocking buffer overnight at 4 °C or for 1 h at room temperature. The membrane was washed in TBS-T, incubated with an anti-rabbit HRP-coupled secondary antibody (Agilent) in TBS-T for 1 h, and washed again in TBS-T. Proteins were detected with the SuperSignal West Pico PLUS Chemiluminescent Substrate (Thermo Fisher) and acquired using an ImageQuant LAS 4000 (GE Healthcare).

### ChIP-seq

Cells were harvested by trypsinization, washed with PBS, crosslinked with 1% formaldehyde in PBS for 10 min, quenched by adding 1/10 volume of 1.25 M glycine for 2 min, and washed twice in ice-cold PBS. Crosslinked cell pellets were stored at −80 °C until extracted in lysis buffer (50 mM Tris HCl pH 8, 10 mM EDTA, 0.5% SDS, 1X protease inhibitors) on ice for 10 min. Lysates were sonicated using a Covaris M220 for 15 min at 4–10 °C with a duty factor of 10%, peak power of 75 W, and 200 cycles/burst. Sonicated lysates were cleared by centrifugation at 16,000 × g for 10 min at 4 °C, and supernatant was collected. Samples were then processed using the SimpleChIP® Plus Sonication Chromatin IP Kit (Cell Signaling). Pulldown using 10 μg of chromatin was performed with 10 μL of H3K27me3 antibody (C36B11, Cell Signaling Technology). Libraries were prepared from 6.5 ng DNA using the KAPA HyperPlus Kit (Roche) according to the manufacturer's protocol, except that the fragmentation step was skipped. DNA libraries were pooled and sequenced on the NovaSeq platform.

### ATAC-seq

ATAC-seq libraries were prepared from 25,000 cells following the Omni-ATAC protocol<sup>52</sup> and using the Tagment DNA Enzyme and Buffer Kit (Illumina). Samples were pooled and run in one HiSeq lane.

### PRO-seq

Nuclei were purified by washing cells twice with cold PBS and incubating them in ice-cold swelling buffer (10 mM Tris-HCl pH 7.5, 2 mM MgCl<sub>2</sub>, 3 mM CaCl<sub>2</sub>) on ice for 15 min. Cells were collected in 20 mL swelling buffer using a cell scraper and centrifuged at 1000 × g for 10 min at 4 °C. Cell pellets were resuspended in 1 mL of lysis buffer (10 mM Tris HCl pH 7.5, 2 mM MgCl<sub>2</sub>, 3 mM CaCl<sub>2</sub>, 0.5% IGEPAL, 10% glycerol, RNase Inhibitor) using a wide-orifice pipette tip. An additional 9 mL of lysis buffer was added, and the mixture was centrifuged at 600 × g for 5 min at 4 °C. This resuspension step was repeated once. The nuclei pellets were then resuspended in 1 mL of freezing buffer (50 mM Tris HCl pH 8.3, 5 mM MgCl<sub>2</sub>, 40% glycerol, 0.1 mM EDTA pH 8.0) and transferred to low-bind microcentrifuge tubes. After centrifugation at 600 × g at 4 °C for 5 min, nuclei pellets were resuspended in 500 μL of freezing buffer and centrifuged at 600 × g for 5 min at 4 °C. Nuclei pellets were finally resuspended in 110 μL of freezing buffer and flash-frozen in liquid nitrogen to be stored overnight at −80 °C.

The nuclear run-on experiments for PRO-seq were performed in triplicate as described previously<sup>53</sup> with the use of a mixture of rNTPs and Biotin-11-CTP (PerkinElmer), and a range of 10–20 million isolated nuclei per sample. Briefly, after the nuclear transcription run-on reaction, total RNA was extracted with TRIzol LS reagent (Thermo Fisher) and then fragmented by base hydrolysis. Biotinylated fragmented nascent transcripts were enriched a total of three times using streptavidin Dynabeads (Invitrogen) and TRIzol LS reagent. The VRA3 RNA adapter was ligated to the 3' end of nascent RNA following the first biotin enrichment. After the second biotin enrichment, the 5' ends of the RNA were enzymatically modified with pyrophosphohydrolase and polynucleotide kinase and then ligated to the VRA5 RNA adapter. Following the third biotin enrichment, a reverse transcription reaction was performed, and the resulting adapter-ligated libraries were purified using AMPure XP beads (Beckman Coulter). The libraries were amplified with eleven cycles of PCR, purified with AMPure beads, pooled, and run on the NovaSeq platform.

### Data analysis

**RNA-seq analysis.** Quality control, read mapping, and quantification was performed using nf-core/rnaseq v1.4.2<sup>54</sup>. Reads were mapped to mm10 and quantified with Salmon v1.5.2<sup>55</sup> using the Gencode M25 annotation.

Static *Ferre*<sup>KO</sup> vs WT analysis: Significantly differentially expressed genes were calculated using DESeq2<sup>56</sup> with an adjusted *p*-value cutoff of 0.05 and a fold change cutoff of 1.5 on the shrunken log<sub>2</sub> fold change values from DESeq2.

Dox control analysis: Differential expression was calculated using DESeq2 and the Wald test to compare each time point back to the zero-time point. The rescue and overexpression dox control lines and the corresponding short and long-time courses were analyzed separately. Cutoffs to call differentially expressed genes were made using an adjusted *p*-value cutoff of 0.05 and whether a gene achieved a fold change > 1.5 at any time point (calculated using the shrunken log<sub>2</sub> fold change).

*Ferre* induction time course analysis: Differential expression was calculated with DESeq2 using the likelihood ratio test to compare a full model which contains the *Ferre* induction/time point interaction term to a reduced model lacking that term. Calling differentially expressed genes proceeded in two steps: (1) A cutoff was made on the adjusted *p*-values from the likelihood ratio test (*p* < 0.05), filtering to genes that

changed significantly in time as compared to the dox control. (2) A fold change cutoff was made by comparing the expression through time back to the zero-time point (without any comparison to the dox control line). A gene was called differentially expressed (responding to *Fire*) if it achieved a fold change  $> 1.5$  in any time point as measured by the shrunken  $\log_2$  fold change from DESeq2.

The combined model using all four cell lines was analyzed in the same manner with the same thresholding strategy, but the full and reduced models contained an additional indicator variable for the *Fire* genotype (WT or KO).

The  $\log_2$  fold changes shown in the heatmaps are the shrunken  $\log_2$  fold changes reported by DESeq2.

**Identification of rescued genes:** A gene was considered rescued, if: (1) It was significantly differentially expressed in the static *Fire*<sup>KO</sup> vs WT comparison and in the *Fire*<sup>RESCUE</sup> induction experiment, and (2) If the fold change was reciprocal to within 20% of the fold change value in the *Fire*<sup>KO</sup> vs WT.

To determine whether any early *Fire* responding genes may result from rtTA activation, publicly available RNA-seq count data were retrieved from the Gene Expression Omnibus (GEO) database for the accession number GSE118898. Specifically, raw RNA-seq count data for the following samples were extracted: (HV\_G1\_SunTag\_Nanog\_A1\_pLif\_mDox\_1, HV\_G5\_SunTag\_Nanog\_E1\_pLif\_mDox\_1, HV\_G7\_SunTag\_Nanog\_E1\_pLif\_mDox\_2, HV\_G4\_SunTag\_Nanog\_A1\_pLif\_pDox\_2, HV\_G6\_SunTag\_Nanog\_E1\_pLif\_pDox\_1).

These samples represent conditions with (pDox) and without dox (mDox) treatment in a mouse embryonic stem cell line (E14Tg2a) containing a dox-inducible *Nanog* transgene. Differential expression analysis between the pDox and mDox conditions was performed using the DESeq2 R package.

**ChIP-seq analysis.** Quality control and read mapping were performed using the nf-core/chipseq v1.1.0 pipeline. Using that pipeline, reads were mapped to mm10 with the mm10 ENCODE Blacklist v2 (<https://github.com/Boyle-Lab/Blacklist/blob/master/lists/mm10-blacklist.v2.bed.gz>) using BWA MEM (v0.7.17-r1188). Consensus peaks were called with MACS v2.2.71 by using all IP conditions as the treatment and all inputs as controls. This was performed with the flags: --broad --broad-cutoff 0.1 -B. Counts over peak regions were calculated using Rsubread's (v2.0.1) featureCounts. To identify differential H3K27me3 peak regions, the DESeq2 (v1.26.0) Wald test was used to compare 48-h *Fire*-induced samples to controls. Significant peaks were those with Benjamini-Hochberg adjusted  $p$ -values  $< 0.05$ .

**ATAC-seq analysis.** Quality control, read mapping, and peak calling were carried out using nf-core/atacseq v1.2.0. Reads were mapped to mm10 and the mm10 v2 blacklist from ENCODE was used. Within the nf-core/atacseq pipeline MACS2 v2.2.7.1<sup>57,58</sup> was used to call peaks in each experiment separately. Consensus peaks were called using the peak regions present in any single experiment. Reads within peaks were calculated using featureCounts. Differentially accessible peaks were calculated using DESeq2 to compare the read counts in the samples in which *Fire* was present ( $>0$  time point in the *Fire*<sup>RESCUE</sup> and *Fire*<sup>OE</sup> lines) and the samples in which *Fire* was absent (WT and *Fire*<sup>KO-CTL</sup> lines, and zero-time points). A cutoff was made using the adjusted  $p$ -value ( $p < 0.05$ ).

**PRO-seq analysis.** Quality control and read mapping were performed using the Nascent-Flow Nextflow pipeline (<https://github.com/Dowell-Lab/Nascent-Flow>). In that pipeline, reads were mapped to mm10 using Hisat2 with the flags --very-sensitive and --no-spliced-alignment. Bidirectionals were called with Tfit using the Bidirectional-Flow pipeline with the default parameters (<https://github.com/Dowell-Lab/Nascent-Flow>). muMerge v1.1.0 (<https://github.com/Dowell-Lab/>

*numerge*) was used to merge bidirectional nascent transcript calls across samples. For quantification, a uniform 600 bp region from the center of the muMerge identified bidirectional was used. Counts in each sample were called using Rsubread's (v2.0.1) featureCounts over these regions. To filter to transcripts that produced reads on both transcripts, featureCounts was used to generate counts over the positive and negative strand aligned reads by using separate 'saf' files over these 600 bp regions with + and - strand regions. Bidirectionals were then filtered to those that had  $\geq 5$  reads on each strand and a strand bias ratio of  $< 1$ . To identify differentially expressed nascent transcripts over the time course, DESeq2 (v1.26.0) was used to calculate a likelihood ratio test between the full model (-timepoint) vs a reduced model (-1). Further, to evaluate the magnitude of expression changes, DESeq2 was run using the Wald test to compare the 15- and 30 min time points to the zero-time point. A transcript was considered significant if the LRT test  $\text{padj} < 0.05$  and achieved  $|\text{fold change}| > 1.5$  in either time point. The metaplot of PRO-seq signal over the 550 differential bidirectional regions was generated by summing the signal over the positive and negative strands separately over all replicates. To detect changes in nascent transcription along the gene body, Rsubread's (v2.0.1) featureCounts was used to quantify counts over the gene body lacking the 5'-most 500 bp so as not to include the promoter bidirectional. Differential expression of nascent transcription in the gene body was performed with DESeq2 (v1.26.0) using a likelihood ratio test over the time points with the full model (-timepoint) and reduced model (-1).

### Statistics and reproducibility

No statistical method was used to predetermine sample size. No data were excluded from the analyses. Data are representative of multiple independent experiments and orthogonal approaches. All samples were allocated randomly into experimental groups. The Investigators were blinded to sample allocation during library preparation.

### Reporting summary

Further information on research design is available in the Nature Portfolio Reporting Summary linked to this article.

### Data availability

All sequencing data generated in this study have been submitted to the NCBI Gene Expression Omnibus (GEO; <https://www.ncbi.nlm.nih.gov/geo/>) under accession number GSE202406. Source data are provided with this paper.

### Code availability

All code to reproduce the analyses is available at: [github.com/msmallegan/fire\\_timecourse](https://github.com/msmallegan/fire_timecourse).

### References

- Andergassen, D. & Rinn, J. L. From genotype to phenotype: genetics of mammalian long non-coding RNAs in vivo. *Nat. Rev. Genet.* **23**, 229–243 (2021).
- Guttman, M. et al. lincRNAs act in the circuitry controlling pluripotency and differentiation. *Nature* **477**, 295–300 (2011).
- Huarte, M. et al. A large intergenic noncoding RNA induced by p53 mediates global gene repression in the p53 response. *Cell* **142**, 409–419 (2010).
- Loewer, S. et al. Large intergenic non-coding RNA-RoR modulates reprogramming of human induced pluripotent stem cells. *Nat. Genet.* **42**, 1113–1117 (2010).
- Guttman, M. & Rinn, J. L. Modular regulatory principles of large non-coding RNAs. *Nature* **482**, 339–346 (2012).
- Wapinski, O. & Chang, H. Y. Long noncoding RNAs and human disease. *Trends Cell Biol.* **21**, 354–361 (2011).



7. Rinn, J. L. & Chang, H. Y. Long noncoding RNAs: molecular modalities to organismal functions. *Annu Rev. Biochem* **89**, 283–308 (2020).
8. Maass, P. G. et al. A misplaced lncRNA causes brachydactyly in humans. *J. Clin. Investig.* **122**, 3990–4002 (2012).
9. Xue, Z. et al. A G-rich motif in the lncRNA braveheart interacts with a zinc-finger transcription factor to specify the cardiovascular lineage. *Mol. Cell* **64**, 37–50 (2016).
10. Chen, Y. G., Satpathy, A. T. & Chang, H. Y. Gene regulation in the immune system by long noncoding RNAs. *Nat. Immunol.* **18**, 962–972 (2017).
11. Engreitz, J. M., Ollikainen, N. & Guttman, M. Long non-coding RNAs: spatial amplifiers that control nuclear structure and gene expression. *Nat. Rev. Mol. Cell Biol.* **17**, 756–770 (2016).
12. Cheng, L., Ming, H., Zhu, M. & Wen, B. Long noncoding RNAs as organizers of nuclear architecture. *Sci. China Life Sci.* **59**, 236–244 (2016).
13. Quinodoz, S. & Guttman, M. Long noncoding RNAs: an emerging link between gene regulation and nuclear organization. *Trends cell Biol.* **24**, 651–663 (2014).
14. Briggs, J. A., Wolvetang, E. J., Mattick, J. S., Rinn, J. L. & Barry, G. Mechanisms of long non-coding RNAs in mammalian nervous system development, plasticity, disease, and evolution. *Neuron* **88**, 861–877 (2015).
15. Wang, K. C. & Chang, H. Y. Molecular mechanisms of long non-coding RNAs. *Mol. Cell* **43**, 904–914 (2011).
16. Yin, Y. et al. Opposing roles for the lncRNA haunt and its genomic locus in regulating HOXA gene activation during embryonic stem cell differentiation. *Cell Stem Cell* **16**, 504–516 (2015).
17. Cho, S. W. et al. Promoter of lncRNA gene PVT1 is a tumor-suppressor DNA boundary element. *Cell* **173**, 1398–1412.e22 (2018).
18. Wang, Z. et al. The long noncoding RNA Chaer defines an epigenetic checkpoint in cardiac hypertrophy. *Nat. Publ. Group* **22**, 1131–1139 (2016).
19. Andersen, R. E. et al. The long noncoding RNA Pnky is a trans-acting regulator of cortical development in vivo. *Dev. Cell* **49**, 632–642.e7 (2019).
20. Lewandowski, J. P. et al. The Firre locus produces a trans-acting RNA molecule that functions in hematopoiesis. *Nat. Commun.* **10**, 5137 (2019).
21. Abe, Y. et al. Xq26.1-26.2 gain identified on array comparative genomic hybridization in bilateral periventricular nodular heterotopia with overlying polymicrogyria. *Dev. Med. Child Neurol. n/a-n/a* **56**, 1221–1224 (2014).
22. Hacisuleyman, E., Shukla, C. J., Weiner, C. L. & Rinn, J. L. Function and evolution of local repeats in the Firre locus. *Nat. Commun.* **7**, 11021 (2016).
23. Hacisuleyman, E. et al. Topological organization of multi-chromosomal regions by the long intergenic noncoding RNA Firre. *Nat. Struct. Mol. Biol.* **21**, 198–206 (2014).
24. Barutcu, A. R., Maass, P. G., Lewandowski, J. P., Weiner, C. L. & Rinn, J. L. A TAD boundary is preserved upon deletion of the CTCF-rich Firre locus. *Nat. Commun.* **9**, 1444 (2018).
25. Bonora, G. et al. Orientation-dependent Dlx4 contacts shape the 3D structure of the inactive X chromosome. *Nat. Commun.* **9**, 1445 (2018).
26. Yang, F. et al. The lncRNA Firre anchors the inactive X chromosome to the nucleolus by binding CTCF and maintains H3K27me3 methylation. *Genome Biol.* **16**, 52 (2015).
27. Fang, H. et al. Trans- and cis-acting effects of Firre on epigenetic features of the inactive X chromosome. *Nat. Commun.* **11**, 6053 (2019).
28. Heurtier, V. et al. The molecular logic of Nanog-induced self-renewal in mouse embryonic stem cells. *Nat. Commun.* **10**, 1109 (2019).
29. Dukler, N. et al. Nascent RNA sequencing reveals a dynamic global transcriptional response at genes and enhancers to the natural medicinal compound celastrol. *Genome Res.* **27**, 1816–1829 (2017).
30. Azofeifa, J. G. & Dowell, R. D. A generative model for the behavior of RNA polymerase. *Bioinformatics* **33**, 227–234 (2016).
31. Chen, E. Y. et al. Enrichr: interactive and collaborative HTML5 gene list enrichment analysis tool. *BMC Bioinform.* **14**, 128 (2013).
32. Kuleshov, M. V. et al. Enrichr: a comprehensive gene set enrichment analysis web server 2016 update. *Nucleic Acids Res.* **44**, W90–W97 (2016).
33. Lee, T. I. & Young, R. A. Transcription of eukaryotic protein-coding genes. *Genetics* **34**, 77–137 (2000).
34. Mitchell, P. J. & Tjian, R. Transcriptional regulation in mammalian cells by sequence-specific DNA binding proteins. *Science* **245**, 371–378 (1989).
35. Thoresen, D. et al. The molecular mechanism of RIG-I activation and signaling. *Immunol. Rev.* **304**, 154–168 (2021).
36. Thoresen, D. T., Galls, D., Götte, B., Wang, W. & Pyle, A. M. A rapid RIG-I signaling relay mediates efficient antiviral response. *Mol. Cell* **83**, 90–104.e4 (2022).
37. Mahat, D. B., Salamanca, H. H., Duarte, F. M., Danko, C. G. & Lis, J. T. Mammalian heat shock response and mechanisms underlying its genome-wide transcriptional regulation. *Mol. Cell* **62**, 63–78 (2016).
38. Koczor, C. A. et al. Temporal dynamics of base excision/single-strand break repair protein complex assembly/disassembly are modulated by the PARP/NAD<sup>+</sup>/SIRT6 axis. *Cell Rep.* **37**, 109917 (2021).
39. Younger, S. T., Kenzelmann-Broz, D., Jung, H., Attardi, L. D. & Rinn, J. L. Integrative genomic analysis reveals widespread enhancer regulation by p53 in response to DNA damage. *Nucleic Acids Res. gkv284* **43**, 4447–4462 (2015).
40. Georgescu, W. et al. Characterizing the DNA damage response by cell tracking algorithms and cell features classification using high-content time-lapse analysis. *PLoS One* **10**, e0129438 (2015).
41. Hsu, P. Y. et al. Estrogen-mediated epigenetic repression of large chromosomal regions through DNA looping. *Genome Res.* **20**, 733–744 (2010).
42. Wissink, E. M., Vihervaara, A., Tipples, N. D. & Lis, J. T. Nascent RNA analyses: tracking transcription and its regulation. *Nat. Rev. Genet.* **20**, 705–723 (2019).
43. Sasse, S. K. et al. Nascent transcript analysis of glucocorticoid crosstalk with TNF defines primary and cooperative inflammatory repression. *Genome Res.* **29**, 1753–1765 (2019).
44. Lambert, S. A. et al. The human transcription factors. *Cell* **172**, 650–665 (2018).
45. Abascal, F. et al. Expanded encyclopaedias of DNA elements in the human and mouse genomes. *Nature* **583**, 699–710 (2020).
46. Carneiro, F. et al. Case report: diffuse polymicrogyria associated with a novel ADGRG1 variant. *Front. Pediatr.* **9**, 728077 (2021).
47. Breitfeld, J. et al. Developmentally driven changes in adipogenesis in different fat depots are related to obesity. *Front. Endocrinol.* **11**, 138 (2020).
48. Sun, L. et al. Long noncoding RNAs regulate adipogenesis. *Proc. Natl Acad. Sci. USA* **110**, 3387–3392 (2013).
49. Much, C. et al. Evolutionary divergence of Firre localization and expression. *Rna* **28**, 842–853 (2022). rna.079070.121.
50. Livak, K. J. & Schmittgen, T. D. Analysis of relative gene expression data using real-time quantitative PCR and the 2<sup>−ΔΔC<sub>T</sub></sup> method. *Methods* **25**, 402–408 (2001).
51. Khong, A. & Parker, R. mRNP architecture in translating and stress conditions reveals an ordered pathway of mRNP compaction. *J. Cell Biol.* **217**, 4124–4140 (2018).
52. Corces, M. R. et al. An improved ATAC-seq protocol reduces background and enables interrogation of frozen tissues. *Nat. Methods* **14**, 959–962 (2017).



53. Mahat, D. B. et al. Base-pair-resolution genome-wide mapping of active RNA polymerases using precision nuclear run-on (PRO-seq). *Nat. Protoc.* **11**, 1455–1476 (2016).
54. Ewels, P. A. et al. The nf-core framework for community-curated bioinformatics pipelines. *Nat. Biotechnol.* **38**, 276–278 (2020).
55. Patro, R., Duggal, G., Love, M. I., Irizarry, R. A. & Kingsford, C. Salmon provides fast and bias-aware quantification of transcript expression. *Nat. Methods* **14**, 417–419 (2017).
56. Love, M. I., Huber, W. & Anders, S. Moderated estimation of fold change and dispersion for RNA-seq data with DESeq2. *Genome Biol.* **15**, 550 (2014).
57. Feng, J., Liu, T., Qin, B., Zhang, Y. & Liu, X. S. Identifying ChIP-seq enrichment using MACS. *Nat. Protoc.* **7**, 1728–1740 (2012).
58. Zhang, Y. et al. Model-based analysis of ChIP-Seq (MACS). *Genome Biol.* **9**, R137 (2008).

## Acknowledgements

We would like to thank Gabrijela Dumbović and Aaron Nguyen for their help with smRNA FISH, Nydia Chang for assistance in deriving the mESCs, and Taeyoung Hwang for his initial guidance in analyzing the *Firre* time course data. We are grateful to Roy Parker and Carolyn Decker for access to, and training on, the DeltaVision Elite microscope. We acknowledge the support of Theresa Nahreini and Nicole Kethley at the Biochemistry Cell Culture Facility, Amber Scott at the BioFrontiers Sequencing Core, and Joe Dragavon at the BioFrontiers Advanced Light Microscopy Core. C.M. was supported by the Deutsche Forschungsgemeinschaft (DFG, MU 4462/1-1). J.R. is HHMI Faculty Scholar and the work was supported by NIH/NIGMS grant P01 GM099117.

## Author contributions

J.L.R., E.L.L., and C.M. conceptualized and designed the study; J.P.L. derived the mESC lines; C.M. and E.L.L. cultured the cells and optimized the time course experiments; C.M. performed RNA-seq, ChIP-seq, ATAC-seq, and smRNA FISH experiments and analyzed microscopy data; I.T.P., T.K.V., and D.R. performed PRO-seq under supervision of R.D.D.; M.J.S. and J.L.R. conducted the computational analyses; J.L.R., C.M., and M.J.S. wrote the manuscript with input from all the authors.

## Competing interests

The authors declare no competing interests.

## Additional information

**Supplementary information** The online version contains supplementary material available at <https://doi.org/10.1038/s41467-024-50402-0>.

**Correspondence** and requests for materials should be addressed to Michael J. Smallegan or John L. Rinn.

**Peer review information** *Nature Communications* thanks Zhen Yang and the other, anonymous, reviewer(s) for their contribution to the peer review of this work. A peer review file is available.

**Reprints and permissions information** is available at <http://www.nature.com/reprints>

**Publisher's note** Springer Nature remains neutral with regard to jurisdictional claims in published maps and institutional affiliations.

**Open Access** This article is licensed under a Creative Commons Attribution-NonCommercial-NoDerivatives 4.0 International License, which permits any non-commercial use, sharing, distribution and reproduction in any medium or format, as long as you give appropriate credit to the original author(s) and the source, provide a link to the Creative Commons licence, and indicate if you modified the licensed material. You do not have permission under this licence to share adapted material derived from this article or parts of it. The images or other third party material in this article are included in the article's Creative Commons licence, unless indicated otherwise in a credit line to the material. If material is not included in the article's Creative Commons licence and your intended use is not permitted by statutory regulation or exceeds the permitted use, you will need to obtain permission directly from the copyright holder. To view a copy of this licence, visit <http://creativecommons.org/licenses/by-nc-nd/4.0/>.

© The Author(s) 2024